Astronomy & Astrophysics

High-resolution optical spectroscopy of V838 Monocerotis in 2009[*],[**]

R. Tylenda[1], T. Kamiński[1],[***], M. Schmidt[1], R. Kurtev[2], and T. Tomov[3]

[1] Department for Astrophysics, Nicolaus Copernicus Astronomical Center, Rabiańska 8, 87-100 Toruń, Poland
e-mail: [tylenda;tomkam;schmidt]@ncac.torun.pl
[2] Departamento de Fisica y Astronomia, Universidad de Valparaiso, Av. Gran Bretana 1111, casilla 5030, Valparaiso, Chile
e-mail: radostin.kurtev@uv.cl
[3] Toruń Centre for Astronomy, Nicolaus Copernicus University, Gagarina 11, 87−100 Toruń, Poland
e-mail: Toma.Tomov@astri.uni.torun.pl

ABSTRACT

Context. V838 Mon erupted at the beginning of 2002. In the course of the outburst the object evolved to low effective temperatures and declined as a very late M-type supergiant. Among various scenarios proposed to explain the nature of the outburst, the most promising is a stellar merger event.
Aims. We aim at studying the structure and evolution of the object in the decline from the 2002 eruption.
Methods. We obtained spectroscopic observations of V838 Mon in January−March 2009 with UVES/VLT. The results are analysed and compared with similar observations obtained in October 2005 with HIRES/Keck.
Results. The most striking difference between 2009 and 2005 is a complete absence of the B3 V component and of the [FeII] emission lines in 2009. The present spectrum displays only the spectrum of the 2002 eruption remnant. It resembles that of an ~M6 giant, although the molecular bands in V838 Mon are deeper than those in standard stellar spectra of a similar spectral class. Several atomic lines, which displayed P-Cyg profiles in 2005, are now dominated by pure absorptions. Some of these lines, however, show a narrow emission component, which, as we argue, measures the radial velocity of V838 Mon. The resulting heliocentric velocity is 71 km s^{-1}, which very well agrees with the velocity obtained from SiO maser observations. The atomic lines and the molecular bands show very complex kinematics. In some atomic lines and high-excitation molecular bands we observe matter infalling in the object atmosphere. The infall components were already observed in 2005, but were less pronounced and present in fewer lines than in 2009. We argue that the most negative radial velocity components seen in the resonance atomic lines and in the low-excitation molecular bands were formed in the ejecta of the 2002 eruption. The B3 V companion most probably became engulfed in an opaque dusty matter of the 2002 V838 Mon ejecta.

Key words. stars: individual: V838 Mon – stars: late-type – stars: peculiar

1. Introduction

The eruption of V838 Mon was observed in January-March 2002 (e.g. Munari et al. 2002a). The object attracted significant public attention, mainly because of its spectacular light echo (Bond et al. 2003). The eruption itself was also very interesting and intriguing. The light curve could have been taken for that of a slow nova, but the colour and spectroscopic evolution of the object suggested a different nature. In the course of the eruption the spectrum evolved to late spectral types and the object declined as a very late M-type supergiant. At present, soon a decade after the eruption, the remnant still shows a spectrum, which can be classified as an ~M6 giant or supergiant.

A few other stellar eruptions show characteristics very similar to those of V838 Mon. They are named "V838 Mon-type objects" or "red novae". Apart from V838 Mon, this class includes M31 RV (Mould et al. 1990), V4332 Sgr (Martini et al. 1999), and V1309 Sco (Mason et al. 2010). Some extragalactic intermediate-lumnosity optical transients, like M85 OT2006 (Kulkarni et al. 2007) and NGC 300 OT2008 (Bond et al. 2009; Berger et al. 2009), probably also belong to this class of stellar eruptions.

The nature of the V838 Mon-type eruptions has not yet been fully explained. As discussed in Tylenda & Soker (2006), thermonuclear mechanisms such as classical nova (Iben & Tutukov 1992) or a late He-shell flash (Lawlor 2005) should be excluded. Instead, Tylenda & Soker (2006) showed that all the main observational characteristics of the V838 Mon-type eruptions can be consistently understood as resulting from stellar collisions and mergers. This idea obtained a strong support from archive photometric observations of the progenitor of V1309 Sco analysed in Tylenda et al. (2011). The data evidently show that the progenitor was a contact binary quickly evolving towards its merger. According to Kashi et al. (2010) and Kashi & Soker (2010), certain optical transients may result from mass transfer events in binary systems.

Table 1. Technical details of the UVES/VLT observation of V838 Mon and the spectrophotometric standard Hiltner 600.

Date	UT	JD–24e5	Object	Exp. time (s)	Airmass	Seeing ($''$)
2009-01-02	05:04:29	54 833.211	V838 Mon	2105	1.07	1.53
2009-01-02	05:56:33	54 833.248	V838 Mon	3005	1.10	1.57
2009-01-02	05:45:50	54 833.240	Hilt 600	305	1.17	1.52
2009-02-13	01:29:13	54 875.062	V838 Mon	3005	1.09	1.57
2009-02-14	03:54:36	54 876.163	V838 Mon	2105	1.19	1.50
2009-02-16	02:58:02	54 878.124	Hilt 600	305	1.18	0.97
2009-03-22	01:32:37	54 912.064	V838 Mon	3005	1.19	0.86
2009-03-23	01:25:30	54 913.059	V838 Mon	2105	1.18	0.63
2009-03-23	02:06:34	54 913.088	Hilt 600	305	1.48	0.74

A B3 V companion of V838 Mon was discovered when the main object declined from the 2002 eruption (Munari et al. 2002b). The companion remained constant in brightness until an eclipse-like event in November−December 2006 (Munari et al. 2007). In 2004, narrow emission lines, predominantly from [FeII], appeared in the spectrum of V838 Mon (Barsukova et al. 2006). The lines strengthened with time and reached a maximum near the 2006 eclipse-like event (Munari et al. 2007). The emission lines were most likely excited by the radiation of the B3 V companion in the matter ejected by V838 Mon in 2002 that approached the companion (Tylenda et al. 2009). The eclipse-like fading of the companion in 2006 was accordingly caused by a cloud of dusty matter crossing the line of sight of the companion (Tylenda et al. 2009).

A few months after the eclipse-like event, the B3 V companion started a new decline, this time slower but significantly deeper and more complex[1]. In contrast to the 2006 event, the second decline of the companion was also accompanied by a decline of the [FeII] emission lines. This indicated that the radiation of the B3 V companion faded not only for the observer but also for the matter flowing by the companion. Thus the event cannot be explained by another dusty cloud crossing the line of sight. The companion was instead engulfed in dense and opaque matter. Two years after the beginning of the decline, last traces of the B3 V companion disappeared from the spectrum of V838 Mon.

In March 2008, a field of V838 Mon was observed by XMM/Newton and a variable X-ray source was detected near the position of the object (Antonini et al. 2010). The X-rays may have resulted either from magnetic activity of the merger remnant or from interactions of the 2002 ejecta with the B3 V companion. No such source was detected in *Chandra* observations obtained a year after the outburst, nor in January 2010.

In October 2005, we obtained a high-resolution spectrum of V838 Mon with the HIRES/Keck instrument (Kamiński et al. 2009). A detailed analysis of that data was made in Tylenda et al. (2009). In the present paper, we report on similar observations that were obtained in January−March 2009 with the UVES/VLT instrument.

2. Observations

2.1. Spectroscopy

V838 Mon was observed with the UVES spectrograph (Dekker et al. 2000) on the Very Large Telescope (VLT) in 2009 in three observing runs: on 2 January, 13−14 February, and 22−23 March. For each run two exposures were obtained with a total exposure time of 85 min. Technical details of the individual exposures, i.e. observation date, UT time and Julian date at the exposure start, integration time, averaged airmass, and average seeing conditions calculated over the exposure time, are given in Table 1. The observations were performed in the UVES standard *red arm 580* setting, which gives a spectral coverage of 4770−6825 Å with an inter-chip gap between 5785 Å and 5820 Å. We used a slit with a width of 0.7 arcsec and the UVES image slicer No. 1. These settings provided a spectral resolution of about $\lambda/\Delta\lambda = 52\,000$.

All spectra were reduced and calibrated in IRAF[2] using standard procedures for Echelle spectra (Willmarth & Barnes 1994). The reduction procedures included bias- and flat-field corrections, removal of scattered light, and spectra extraction with background subtraction. Cosmic ray events were rejected from the CCD frames with the *Laplacian cosmic ray identification* algorithm (van Dokkum 2001). Observations were wavelength-calibrated using spectra of Th-Ar lamps, and dispersion solutions were fitted to identified lines with a typical accuracy of rms = 3 mÅ. Flux calibration was based on observations of the spectrophotometric standard star Hiltner 600 and its spectrophotometric fluxes tabulated every 50 Å in Hamuy et al. (1994, 1992). We asses the overall accuracy of the relative flux calibration to be about 5%, but it is slightly poorer within strong telluric absorption bands and in spectral regions corresponding to the broad Balmer lines in the spectrum of the standard star. The flux calibration of the spectra from 24−25 March was based on standard-star observations on 26 March and therefore the absolute flux calibration of the March spectra is most uncertain. All spectra were shifted to the heliocentric rest frame, and all Echelle orders from two expositions obtained in the same run were merged into one spectrum. The signal-to-noise ratio reaches a value of 120 in the spectral region with the highest flux level.

In order to check the accuracy of the absolute flux calibration of our spectra, we estimated their corresponding *V* magnitudes by integrating the spectra convolved with the response curve of the *V* filter. The inter-chip gap was interpolated with the shape of the spectrum reported in Kamiński et al. (2009) as a reference. The magnitudes derived from the spectra obtained in January, February, and March are 15.4, 15.5, and 15.3, respectively. They can be compared to the *V* values of 15.36 and 15.34 derived

---

[1] See http://jet.sao.ru/jet/~goray/.

[2] IRAF is distributed by the National Optical Astronomy Observatories, which are operated by the Association of Universities for Research in Astronomy, Inc., under cooperative agreement with the National Science Foundation.

Table 2. Results of the photometric measurements of V838 Mon in 2008−2009.

Date	JD	Band	Mag	Error	Observat.
18 Dec. 2008	2 454 819.45	V	15.36	0.02	SAAO
18 Dec. 2008	2 454 819.45	I_C	10.08	0.10	SAAO
13 Feb. 2009	2 454 876.40	J	7.43	0.13	TCS
13 Feb. 2009	2 454 876.40	H	6.25	0.24	TCS
13 Feb. 2009	2 454 876.40	K_S	5.50	0.07	TCS
16 Mar. 2009	2 454 906.52	B	19.11	0.13	CTIO
16 Mar. 2009	2 454 906.53	V	15.34	0.05	CTIO
16 Mar. 2009	2 454 906.54	R_C	12.63	0.06	CTIO
16 Mar. 2009	2 454 906.55	I_C	10.28	0.12	CTIO
05 Oct. 2009	2 455 109.64	B	18.58	0.66	SAAO
05 Oct. 2009	2 455 109.63	V	15.74	0.28	SAAO
05 Oct. 2009	2 455 109.63	I_C	10.02	0.15	SAAO
06 Oct. 2009	2 455 110.63	B	18.69	0.43	SAAO
06 Oct. 2009	2 455 110.62	V	15.65	0.39	SAAO

from our photometric measurements made in December 2008 and March 2009, which we described in Sect. 2.2 (see Table 2).

The three spectra from January, February, and March have essentially the same shape. However, they are systematically shifted towards each other on the flux scale. The flux level in the spectrum from February is on average $7 \pm 2\%$ lower than that of the spectrum from January, and the last spectrum from March is $14 \pm 2\%$ brighter than the spectrum from January. These flux variations are within the accuracy of the absolute flux calibration of our spectra. We can conclude that the object had essentially the same flux level in the three observations. Minor differences between the three spectra related to individual features are discussed in Sect. 3.4. We have summed up the three spectra and present and analyse the resulting spectrum.

2.2. Photometry

V838 Mon was measured in the optical photometric bands several times in 2008−2009. On 18 December 2008 the object was observed in the V and I_C filters using a CCD camera at the 1 m telescope of the South African Astronomical Observatory (SAAO). Photometric observations were also carried out on 16 March 2009 in the BVR_CI_C filters with the 1 m SMARTS telescope of the Cerro Tololo Inter-American Observatory (CTIO). Finally, a BVI_C photometry was performed on 5−6 October 2009 with the 1 m SAAO telescope.

All the above observations were reduced in IRAF using standard procedures. The magnitudes of V838 Mon were derived using photometry of field stars from Munari et al. (2002a). It should be noted, however, that the quality of the photometry in Munari et al. was questioned in Afsar & Bond (2007), which could introduce some extra systematic errors to our photometry. Magnitudes corresponding to different exposures from the same observing night were averaged for each filter. The results are given in Table 2, where errors are also provided; they include the $3 \times$ rms (root mean square) scatter in magnitudes of different exposures during the night and the $3 \times$ rms uncertainty in the transformation factors. In 2008 V838 Mon became the brightest I_C source in the field of Munari et al., making its calibrations uncertain in this band.

Near-infrared (NIR) photometric observations of V838 Mon in the JHK_S bands were carried out on 13 February 2009 with

the CAIN-3 camera installed on the 1.52 m *Carlos Sánchez* Telescope (TCS)[3]. The date of the NIR observations is the same as that of the second spectroscopic observing run at UVES/VLT. Data were reduced using CAIN data reduction scripts[4] developed in IRAF by the Instituto de Astrofísica de Canarias. The instrumental magnitudes were converted to the standard system using observations of two standard stars FS 11 and FS 18. Their NIR magnitudes were taken from a list of the UKIRT faint standard stars (Casali & Hawarden 1992). The resulting averaged NIR magnitudes for V838 Mon are presented in Table 2.

3. Results, analysis, and comparison to the spectrum obtained in October 2005

3.1. Spectral features

A high-resolution spectrum of V838 Mon in its post-outburst phase was presented in Kamiński et al. (2009) and analysed in Tylenda et al. (2009). This was a HIRES/Keck spectrum obtained in October 2005, i.e. a year before the eclipse-like event observed in November/December 2006 (see, e.g. Munari et al. 2007). A detailed atlas of spectral features in that spectrum can be found in Kamiński et al. (2009). Most of the identified features there are also present in the 2009 UVES/VLT spectrum analysed in this paper. The 2009 spectrum is compared to the 2005 one in Fig. 1.

The complete absence of the spectrum of the B3 V companion and of the [FeII] emission lines in the 2009 spectrum is the most striking difference between the two spectra. These spectral components were best observed in the blue part of the 2005 spectrum, which, i.e. $\lambda < 4750$ Å, was not observed in 2009. Nevertheless, from the available data we can quite firmly conclude that the B3 V component disappeared. Firstly, in 2009, we do not see any trace of the broad $H\beta$ absorption line, which was prominent in 2005 (see Fig. 1). Secondly, in the deep, heavily saturated TiO bands, i.e. at ~4950 Å, 5850−5910 Å or 6160−6230 Å, we saw a residual flux in 2005, which was nicely intepreted as the continuum from the B3 V companion. In the 2009 spectrum the flux in these regions goes practically to a zero level, i.e. significantly below the 2005 level (see Fig. 1). Comparing the observed fluxes in these regions, we can conclude that in 2009 the B3 V spectral component was at least 30 times fainter than in 2005.

As mentioned above, the emission features, which were present in 2005, are not seen in the 2009 spectrum. We have not found any remnant emissions at the positions of the [FeII] lines, which were strong in 2005. Comparing the observed fluxes in the regions of the strongest [FeII] emission lines in 2005, we can conclude that these lines in 2009 are at least 20 times fainter than in 2005.

The emission components of the resonance lines showing P-Cyg profiles in 2005 also became very faint or disappeared completely in 2009. Similarly, the emission band of ScO near 6460 Å is not seen now. The only emission feature, which is clearly present in the 2009 spectrum, is that of the $H\alpha$ line (see Figs. 1 and 3d).

Almost all the atomic absorptions found in 2005 are present in the 2009 spectrum. Their profiles, however, changed considerably (see Sect. 3.3). In addition, the present spectrum displays

Fig. 1. Average spectrum obtained with UVES/VLT in January–March 2009 (black line) is compared to the spectrum obtained with HIRES/Keck (grey line) in October 2005. The spectra are dereddened with $E_{B-V} = 0.9$ and $R_V = 3.1$, and smoothed. A synthetic spectrum of a B3 V star, which contributes to the 2005 fluxes, is shown for comparison (blue line). The UVES spectrum was shifted in fluxes by the values corresponding to the average contribution of the B3 V companion in the 2005 spectrum; the value of the shift is 0.21 for the two top panels, and 0.10 for the other panels. Identified atomic spectral features are indicated by red markers, while molecular band-heads are assigned green markers. The ordinate units are 10^{-13} erg s^{-1} cm^{-2} Å^{-1}.

several absorption features of FeI, TiI, VI, and CrI, which were very weak or absent in 2005. These lines belong to multiplets with lower energy levels of ≲1.1 eV.

In 2009, V838 Mon shows a very rich molecular spectrum in absorption. Practically, all the features identified in the atlas of Kamiński et al. (2009) are present in the UVES spectrum. Some of the bands are more clearly seen in the 2009 spectrum, which allowed us to improve their identification. The shapes and strengths of some of the bands have changed and this is described in detail in Sect. 3.6. In general, many of the strongly saturated bands of TiO are now seen to be less saturated.

Certain spectral regions of the UVES spectrum were not covered in the 2005 spectrum. Identifications of spectral features in these regions can be found in Fig. 1. These ranges give access to two strong lines of BaII $\lambda\lambda$ 4934 and 6496, and absorption bands of AlO (the B–X system) and TiO (the γ' system).

3.2. Spectral energy distribution

We compared the 2009 spectrum with UVES spectra of red giants from the Paranal Atlas (Bagnulo et al. 2003). When the whole spectrum is taken into account, the best fitting spectra have types of *M*6 ± 2. Although the reference spectra
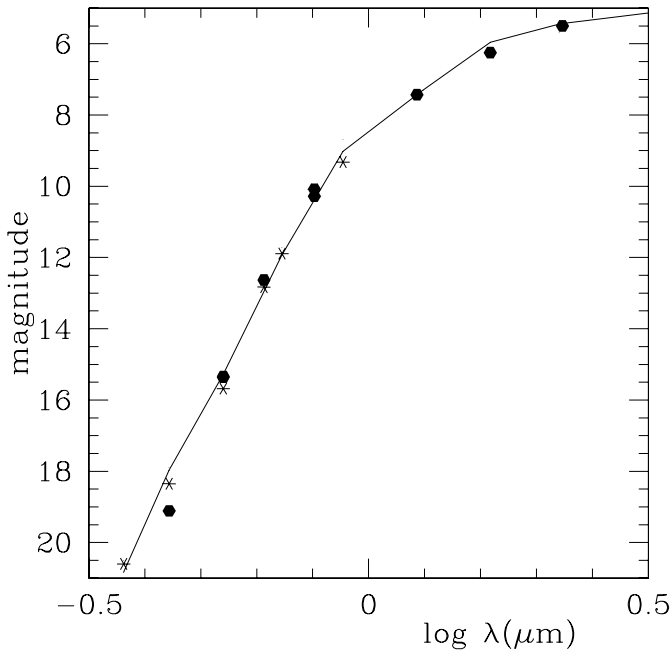
Fig. 2. Standard supergiant photometric spectrum (M6.3 reddened with $E_{B-V} = 0.9$: full line) fitted to the photometric results obtained in December 2008–March 2009. Full points: our data presented in Table 2, asterisks: mean values from the data compiled by V. Goranskij. See text for more details.

reproduce the spectrum of V838 Mon quite well in the regions with a strong pseudo-continuum, numerous absorption bands are significantly deeper in V838 Mon. The same was observed in 2005 (Tylenda et al. 2009).

As can be seen from Fig. 1, V838 Mon in 2009 was significantly brighter than in 2005. After removing the flux of the B3 V star from the 2005 spectrum, we found that the flux of V838 Mon itself in the observed spectral region increased by a factor of ∼2 between 2005 and 2009. This growth in the optical flux was caused by slight increase of V838 Mon in the effective temperature and luminosity (see below), as well as a lower blanketing in the molecular bands in 2009 (see Sect. 3.6).

We fitted standard broad-band photometric spectra to our photometric measurements obtained in December 2008–March 2009 supplemented with mean values taken from the measurements obtained in the same time period that were compiled by V. Goranskij[1] (for details of the fitting procedure see Tylenda 2005). Figure 2 shows the best fit of supergiant (luminosity class I) standards reddened with $E_{B-V} = 0.9$ to the photometric data. The spectral type of the fitted supergiant is M6.3, which agrees well with the spectral type from comparing the Paranal spectra to that of V838 Mon, derived above. This spectral type (M6.3 I) corresponds to an effective temperature of ∼3270 K (Levesque et al. 2005). For a distance of 6.5 kpc (Afsar & Bond 2007; Kamiński et al. 2007; Sparks et al. 2008) the object has an effective radius of ∼380 $R_\odot$ and a luminosity of ∼1.5×10^4 $L_\odot$. Practically the same parameters are obtained when fitting standard giant (luminosity class III) photometric spectra. When compared to the results of a similar analysis made in Kamiński et al. (2009)[5], in 2009 V838 Mon was slightly hotter and ∼20% more luminous than in 2005.

---

[5] Note that in Kamiński et al. (2009) the effective temperature was derived following the spectral type vs. effective temperature calibration

3.3. Profiles of atomic lines

The atomic lines observed in our spectrum show complex structures in their profiles. Examples are shown in Fig. 3. In the following, we assume that the stellar radial velocity is equal to the value derived form SiO masers (Deguchi et al. 2005; Claussen et al. 2007), i.e. $V_h \simeq 71$ km s^{-1} shown with a dashed line in Fig. 3. This point is further discussed in Sect. 3.5. All radial velocities given in this paper are in the heliocentric rest frame.

As discussed in Kamiński et al. (2009), many resonance atomic lines in the spectrum of V838 Mon taken in October 2005 showed P-Cyg profiles. All these lines (except KI λ 7698, RbI λ 7800, and MgI λ 4571, which are outside the wavelength range of the present spectrum) are observed in the 2009 spectrum, but no more as P-Cyg ones; their emission components practically disappeared. The absorption component in many lines is now wider. It is usually more extended towards longer wavelengths, which is at least partly due to the disappearance of the emission component. Some absorptions are shifted to shorter wavelengths, but never beyond the maximum blueshifted absorption observed in 2005. The maximum outflow velocity of ≃215 km s^{-1}, derived from the 2005 spectrum (Tylenda et al. 2009), remains practically the same in 2009.

The absorption lines show complex profiles in most cases. A relatively narrow absorption centred at $V_h \simeq 87$ km s^{-1} (see Fig. 3) is one of the most characteristic features seen in the majority of the lines. In the 2005 spectrum, this component was seen in the TiI lines (Kamiński et al. 2009) and was interpreted as a signature of an infall in the V838 Mon atmosphere (Tylenda et al. 2009). The wings of this feature in the TiI lines are now observed at practically the same velocities as in 2005, but the feature is now deeper and the maximum absorption is at a slightly higher velocity.

The infall component is the only feature seen in the VI lines (see panel h in Fig. 3). These are lines arising from levels with excitation energies as high as ∼1.05 eV. When fitted with a Gaussian, the component has a full-width-at-half depth (FWHD) of ∼15 km s^{-1}. We note that the VI lines were also seen in the 2005 spectrum, but they were then significantly weaker and their profiles were more noisy. Therefore, these lines were not analysed in Kamiński et al. (2009) and Tylenda et al. (2009). Comparing the 2005 spectrum with the present one we can now state that in 2005 the VI lines were of similar width but at slightly lower radial velocities than in 2009. This is consistent with the analysis of the infall component in the TiI lines, presented above.

The profiles of non-resonance FeI lines (panel e in Fig. 3) show a maximum absorption at velocities consistent with the infall. However, they are wider than the profiles of the VI lines and considerably asymmetric. The blue wing extends well below the stellar velocity, indicating an outflow. Contrary to resonance FeI lines (displayed in panel a in Fig. 3) the non-resonance lines do not show any significant feature at $V_h \lesssim 20$ km s^{-1} (structures seen in panel e of Fig. 3 at these velocities are caused by molecular bands).

The infall component in the lines of MnI and CrI (panels f and g in Fig. 3) is separated from the blueshifted (indicating outflow) part of the absorption profile by a narrow emission-like feature peaking at the stellar velocity. In Sect. 3.5 we show that this is most likely a real emission feature.

Clear outflow components, i.e. absorptions at $V_h \lesssim 50$ km s^{-1} are primarily seen in lines arising from levels of low excitation

---

of Schmidt-Kaler (1982). With the calibration of Levesque et al. (2005) the effective temprature in 2005 would have been ∼3200 K.
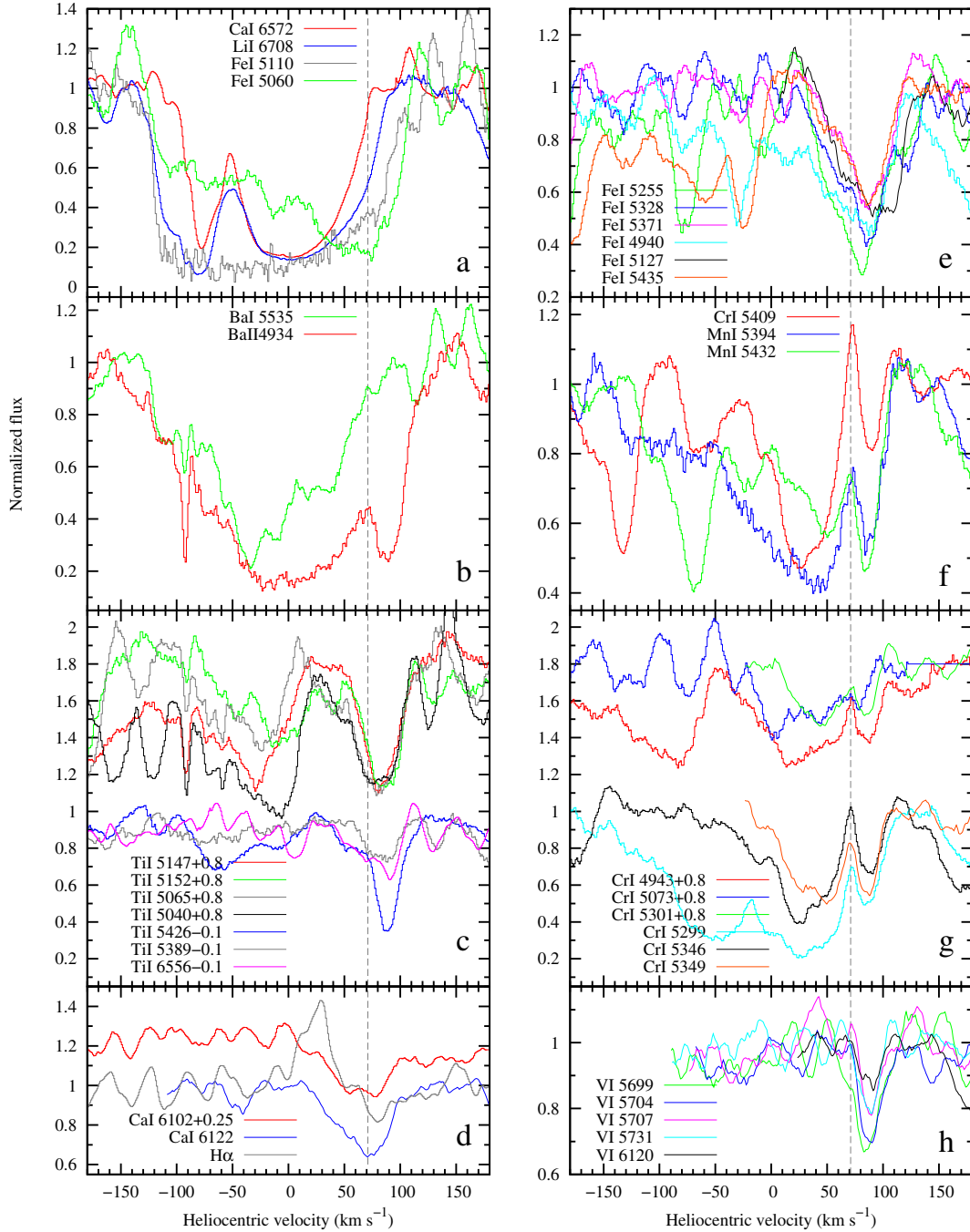
Fig. 3. Sample of profiles of atomic lines in the average UVES spectrum from 2009. The vertical line marks the velocity of the maser of V838 Mon. Some profiles were shifted in ordinate for more clarity. Many structures, particularly seen at negative radial velocities, are caused by blending molecular bands.

energy, i.e. ground states (CaI, LiI, FeI: panel a in Fig. 3; BaI, BaII: panel b; MnI: panel f) and levels with energies $\lesssim 0.05$ eV (TiI lines in panel c)[6]. They are also seen in the CrI lines (panels f and g), however, which arise from levels of energies as high as ~1.0 eV, i.e. excitation energies similar to those of the VI lines, which do not show any outflow (panel h).

In the 2005 spectrum, a relatively narrow absorption component (NAC) was observed at $V_h \simeq -82$ km s^{-1} (see Fig. 6 in Kamiński et al. 2009). It was particularly pronounced in RbI λ 7800 and MgI λ 4571, but also present in MnI λ 5394 and

5432. The two former lines are, unfortunately, outside the spectral range of the present spectrum, but the MnI lines do not show any clear feature at the above velocity in 2009. However, an absorption component at practically the same velocity is now observed in CaI λ 6572 and LiI λ 6708 (see panel a in Fig. 3 and Fig. 4). In 2005, these two lines presented rather smooth absorption profiles extending down to $V_h \simeq -120$ km s^{-1}. The 2009 component is wider, however, than the similar feature in 2005, particularly in LiI λ 6708.

In the 2009 spectrum, we can easily identify a very narrow absorption component at $V_h \simeq -92$ km s^{-1}. It is well seen in the BaI, BaII, and TiI lines (panels b and c in Fig. 3), but a trace of it seems to be also present in the blue wing of the wider feature in

---

[6] There is a mistake in Kamiński et al. (2009) and Tylenda et al. (2009), where the upper energy level of the TiI lines was given as the lower one.
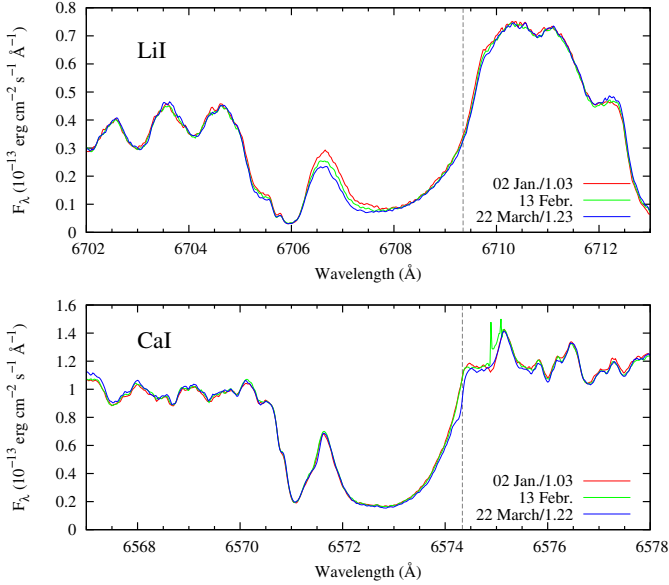
Fig. 4. Spectral variability in the profiles of the LiI λ 6707 and CaI λ 6572 lines as seen in our three UVES spectra from 2009. The January and March spectrum were rescaled to fit the local pseudo-continuum in February. The feature at around 6575 Å in the February spectrum caused by a cosmic-ray hit. The vertical dashed line marks the object heliocentric velocity of 71 km s^{-1}.

the CaI and LiI lines (panel a in Fig. 3). This very narrow feature has a Gaussian profile with $FWHD = 5.6$ km s^{-1}, which is the same as the $FWHM$ of the instrumental profile. A similar feature was observed in 2005 in the TiI lines, but at $V_h = -90$ km s^{-1}. It was also wider than now, but mostly because of the lower resolution of the 2005 spectrum.

The CaI λ 6102 and 6122 lines arise from the highest energy levels ($\sim$1.9 eV)[7] among the lines identified in the 2009 spectrum. Consequently, they are likely to be formed deeply in the photosphere. This is supported by their central positions being close to the stellar velocity (see panel d in Fig. 3). Their wings, extending from $V_h \simeq 10$ km s^{-1} to $V_h \simeq 100$ km s^{-1}, show an outflow and infall in the atmosphere of V838 Mon.

The only clear emission line seen in the 2009 spectrum is that of Hα (see panel d in Fig. 3). The observed position of the line gives $V_h \simeq 29$ km s^{-1}. The line is narrow with $FWHM \simeq 25$ km s^{-1}. The approximate line equivalent width (EW) and dereddened flux are -0.24 Å, and 3.3×10^{-14} erg cm^{-2} s^{-1}, respectively. This feature was absent from the 2005 spectrum.

3.4. Variability on a time-scale of months

A characteristic flow time-scale of the outflow in V838 Mon is $\tau \simeq R_\star/V_{exp} \simeq 20$ days (for $R_\star \simeq 400\ R_\odot$ and $V_{exp} \simeq 150$ km s^{-1}), which is approximately the time span between our three observing runs. Certain differences in individual line profiles can be noticed between these three spectra. The changes are most pronounced in the LiI λ 6707 line, which is expected to have the lowest optical depth among the strong absorption lines. The variability in LiI line is shown in the top panel of Fig. 4. The feature between the deep absorptions appears to slightly decrease with time. Interestingly, the profile of the

---

[7] There is a mistake in Kamiński et al. (2009), where the upper energy level of these CaI lines was given as the lower one.

intercombination line of CaI λ 6572, which exhibits a similar shape as LiI λ 6707, has not undergone similar changes; it shows instead only a minor change in the March spectrum when the absorption profile at around the maser velocity became slightly deeper than in the two earlier epochs (see bottom panel in Fig. 4). Other lines do not show any clear signs of variability above their local noise levels.

3.5. Emission in atomic lines at the stellar velocity

The profiles of many lines displayed in Fig. 3 show an emission-like component at the radial velocity of the SiO maser (71 km s^{-1}). This is particularly the case for the MnI and CrI lines. This can be a real emission, in some sense a remnant of the P-Cyg emission component observed in 2005. Another possibility is that the whole profile is purely absorptive, but the higher flux near the maser velocity simply means that there is little absorbing matter at these velocities.

The case of the CrI λ 5409 (see panel f in Fig. 3), where the emission-like component peaks slightly above the continuum level, argues in favour of the former possibility. Additional arguments arise from comparing profiles of pairs of lines with the same lower energy level, but different oscillator strengths (transition probabilities). This is the case, for instance, for CrI λ 5346 and λ 5349. Both lines have the same lower level, but the former one has a gf-value twice higher than the latter. In the case of pure absorption, the λ 5346 line is expected to be deeper than the λ 5349 one. Panel g in Fig. 3 shows that this is indeed the case except for radial velocities $\lesssim$ 50 km s^{-1}. For higher velocities, in particular in the vicinity of the maser velocity, the situation is reversed, i.e. the flux in the λ 5346 line is higher than in the the λ 5349 one. The emission-like component is clearly stronger in the former line. This shows that the emission-like component at $V_h = 71$ km s^{-1} is indeed of emission origin. The same conclusion can be drawn when comparing the MnI λ 5394 and λ 5432 lines (panel f in Fig. 3). Both lines have the ground level as their lower level, but the former one has a gf-value almost three times higher than the latter. Even the profiles of FeI λ 5110 and λ 5060 (see panel a in Fig. 3), although they do not display any clear emission component, show that the high-velocity regions are affected by emission. These two lines arise from the ground state, but the λ 5110 has a transition probability almost 40 times higher than the λ 5060. For $V_h \lesssim 50$ km s^{-1} the former line is considerably deeper than the latter one, but for $V_h \gtrsim 50$ km s^{-1} the opposite is observed.

We can state, therefore, that an emission component is observed in some atomic lines. This is probably a residual emission component of the P-Cyg profiles observed in 2005 and is most likely produced in the moving (outflowing and/or infalling) matter above the photosphere that is observed above the photospheric limb. The extent of the emitting region is probably small compared to the photospheric radius and therefore, we mainly observe matter moving perpendicularly to the line of sight in the emission component. Hence, the emission is expected to be observed at radial velocities close to the radial velocity of the object. Indeed, the observed emission component is relatively narrow and peaks at a velocity very close to that of the SiO maser (Fig. 3).

This is the first reliable and precise measurement of the radial velocity of V838 Mon obtained from optical spectroscopy. The result agrees very well with that derived from the SiO maser observations. In conclusion, the heliocentric radial velocity of V838 Mon is $V_h = 71$ km s^{-1}.
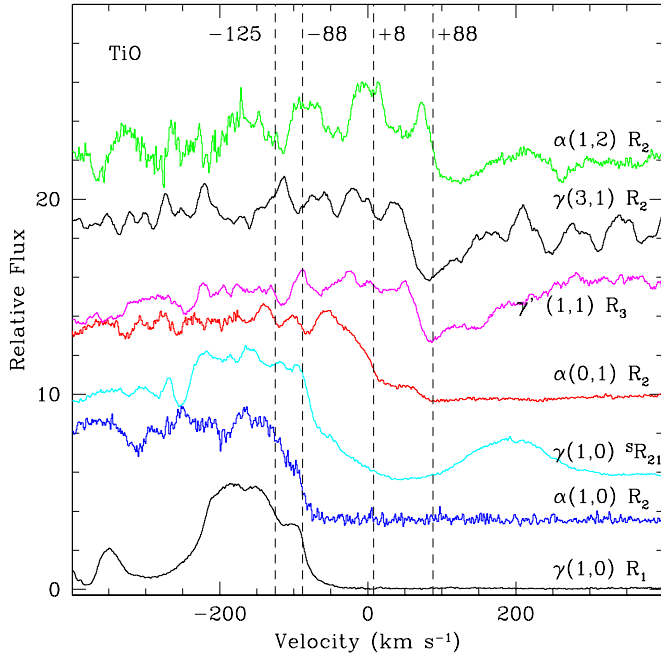
Fig. 5. Sample of the TiO band-heads illustrating the observed velocity components marked with dashed vertical lines. The radial velocity is in the heliocentric frame.

3.6. Molecular bands

The molecular absorption features in the presented spectrum are very similar to those observed in 2005 (Kamiński et al. 2009). We identified bands of TiO, VO, ScO, YO, and AlO. Most of the molecular bands are significantly deeper than in standard stars of a similar spectral type to V838 Mon. However, in the present spectrum, they are mostly observed to be weaker than in the 2005 one. Similarly as in Kamiński et al. (2009), when interpreting the observed band shapes, simulations of a homogeneous absorbing layer situated above the stellar photosphere were performed. Usually, a velocity dispersion of $10-20$ km s^{-1} has to be adopted in the simulations to reproduce the shapes of individual absorption features. Therefore, estimates of the radial velocity from the bands have a typical uncertainty of ~10 km s^{-1}. We do not present detailed figures comparing the results of the simulations with the observed profiles, since they are similar to those shown in Kamiński et al. (2009). Detailes of the molecular bands, for which we were able to derive radial velocities, are given in Appendix A.

3.6.1. TiO

As can be seen from Fig. 5, different TiO bands show different radial velocities. From the bands with relatively sharp heads we were able to identify four velocity components, i.e. -125, -88, 8, and 88 km s^{-1}, which are marked in Fig. 5. A general trend is very similar to that observed in Tylenda et al. (2009, see their Figs. 3 and 4), namely that bands from low excitation levels are seen at low (negative) velocities, while the absorptions from excited vibrational levels show high (positive) velocities. The only important difference is that the highest radial velocity is now observed to be ~88 km s^{-1}, instead of ~58 km s^{-1} as in 2005.

The most negative component, i.e. -125 km s^{-1}, is the same as in 2005 (Kamiński et al. 2009) and is observed only in bands absorbing from the ground vibrational state of the TiO system.
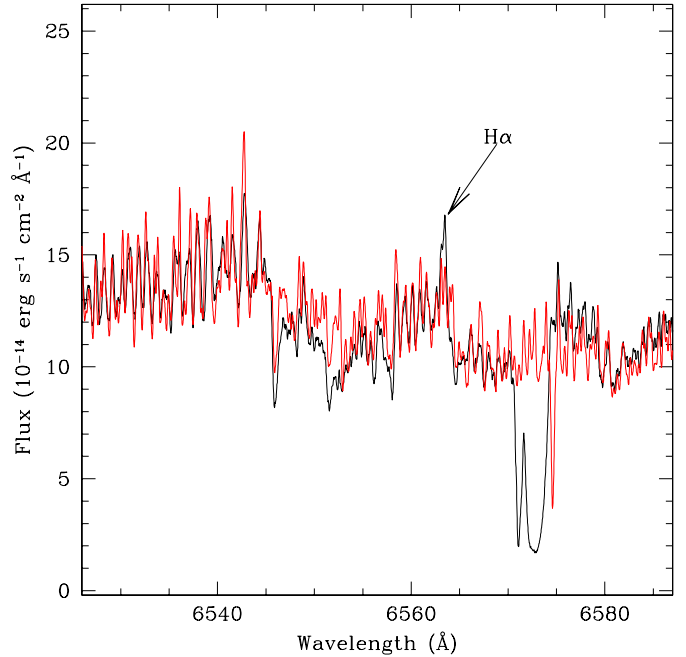

Fig. 6. Part of the 2009 spectrum showing details of highly excited rotational lines of the TiO γ (5, 3) and (6, 4) bands. The V838 Mon spectrum (in black) is overlaid with an M5 III spectrum (in red). The latter spectrum was shifted to a heliocentric radial velocity of 88 km s^{-1}. A narrow Hα emission line and a broad CaI absorption profile can be recognized in the spectrum of V838 Mon.

The -88 km s^{-1} component is seen in the bands absorbing from the ground vibrational level of TiO, as well as of VO C-X (0, 0) and ScO A-X (0, 0). The component at 8 km s^{-1} is particularly well seen in the AlO bands and is discussed below.

The most redshifted component at 88 km s^{-1} is observed in the excited bands, not only in their heads, but also in their resolved rotational lines. An example is shown in Fig. 6, where a portion of the V838 Mon spectrum is overlaid with a standard M5 III spectrum (taken from Bagnulo et al. 2003). An excellent fit of the positions of the TiO rotational lines in both spectra was obtained when the comparison spectrum was shifted to a heliocentric radial velocity of 88 km s^{-1}. This velocity is observed in practically all highly-excited (from the higher vibrational levels or high-J levels) and weak absorption bands of TiO. Note that this is the same velocity as that of the infalling components observed in numerous atomic lines, as discussed in Sect. 3.3.

Similarly as in Kamiński et al. (2009), an estimate of the excitation temperature of molecular bands can be obtained from fitting the results of our simulations to the observed band shapes. The shape of the TiO γ (1, 0) band can be well reproduced by a layer of gas excited to ~500 K. To reconstruct the shape of the band (2, 1) absorbing from the first excited vibrational levels a higher value must be assumed, i.e. above 750 K. Thus the excitation conditions of the TiO bands are similar to those in 2005 (see Kamiński et al. 2009), indicating that the bands showing a high blueshift are formed well above the photosphere. A column density estimated from the TiO γ (1, 0) band is now a factor of 2 lower than in 2005.

3.6.2. ScO

The shape of two components of the ScO $A^2\Pi$–$X^2\Sigma^+$ (0, 0) band is very similar to that observed in 2005. The simulations show that one cannot derive a single value of the excitation temperature from the observed contour. The head formed by lines absorbing from highly excited levels, i.e. $^RR_{1G}$ at 6064.31 Å, needs an excitation temperature above 750 K, and is formed at a velocity of 66 km s^{-1} (45 km s^{-1} in October 2005). The dominant round absorption contours at 6042 and 6082 Å, formed by the Q and P branches, indicate velocities as low as -10 km s^{-1} and an excitation temperature below 350 K. The features of the A–X (0, 0) band, formed by the $^RR_{2G}+^RQ_{2G}$ and $^QQ_{1G}+^QR_{1G}$ heads, have velocities of about -55 km s^{-1}. This velocity component was also observed in the 2005 spectrum, but now it indicates a lower column density. An additional velocity component at -30 km s^{-1} can be recognized in the discussed heads in the present spectrum.

The ScO A–X (0, 1) band, observed in emission at 6410 and 6460 Å in 2005, is not seen in the present spectrum, neither in emission nor in absorption.

3.6.3. YO

The YO subband of $A^2\Pi$–$X^2\Sigma^+$ (0, 0) at 5975 Å is well reproduced when assuming an excitation temperature in the range of 350–500 K. The velocity of the absorbing gas is then about 16 km s^{-1}. Similarly, from the fit to the second subband at 6135 Å one can infer an excitation temperature of $\sim$350 K and a velocity of 36 km s^{-1}. Both the excitation temperature and the column density are similar to those obtained from the 2005 spectrum (Kamiński et al. 2009). However, in 2005, the YO band components were observed at a velocity of –8 km s^{-1}.

3.6.4. VO

In the observed spectral range only vibrational bands of the VO $C^4\Sigma^-$–$X^4\Sigma^-$ electronic system are observed. In two bands, i.e. (0, 0) at 5735 Å and (1, 0) at 5468 Å, absorbing from the ground level, three velocity components can be inferred from their shapes. The most blueshifted narrow feature is at –74 km s^{-1}. A less clear and dispersed in velocity component is observed in a range of –20 to –40 km s^{-1}. Another component dominating the redward part of the band has a velocity of 20 km s^{-1}. A less intense VO C–X (2, 0) head is observed at a velocity of about 6 km s^{-1}, but here also an extension of absorption towards negative velocities is evident.

In 2005, a velocity component of –77 km s^{-1} was observed in the (1, 0) and (0, 0) bands (Kamiński et al. 2009). Within the limits of uncertainty we can identify it with the –74 km s^{-1} component in the present spectrum. From our simulations of the (0, 0) band in 2009, we can infer an excitation temperature of $\sim$300 K, i.e. a similar value as that obtained in 2005. However, the column density in 2009 decreased by at least a factor of 2 compared to the result from the 2005 spectrum.

3.6.5. AlO

Contrary to TiO, the observed AlO bands have generally very sharp heads if they are absorbing from excited vibrational levels. A sample of the AlO band heads is shown in Fig. 7. Our analysis of them can be summarized as follows.
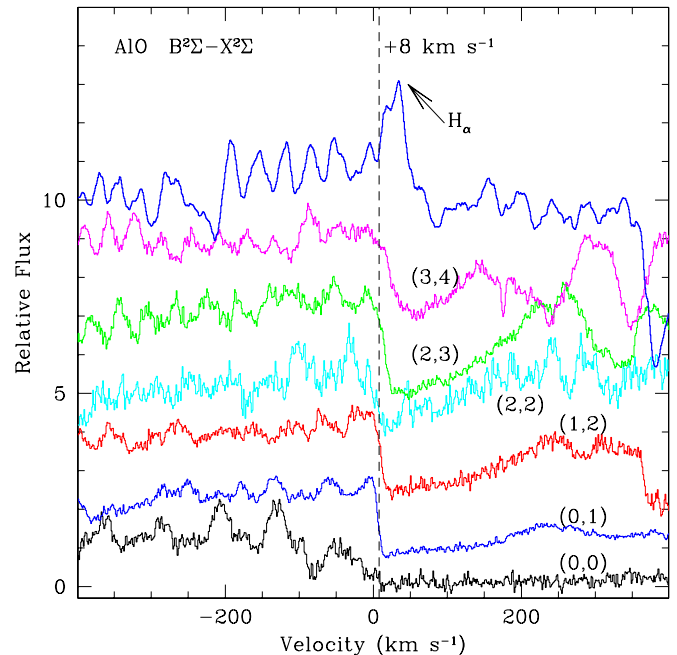

Fig. 7. Detailed view of the AlO $B^2\Sigma$–$X^2\Sigma$ band-heads in the velocity scale (heliocentric frame). The characteristic velocity of 8 km s^{-1} is marked with the vertical dashed line. The Hα emission is also shown at the top of the figure.

– In the spectral range of the present spectrum there is only one band of AlO $B^2\Sigma$–$X^2\Sigma$ originating from the ground vibrational level, (0, 0), at 4842 Å. The head of this band is blended with TiO band rotational lines. Apparently, the band-head extends in velocity from the minimum of absorption at 16 down to at least –100 km s^{-1}.
– All AlO B–X bands originating from excited vibrational levels have sharp band-heads at $\sim$8 km s^{-1}, with a tendency to shift up to $\sim$25 km s^{-1} with the increasing vibrational number of the lower level.
– A regular pattern of the rotational transitions formed by blends of two main P-branches can be easily recognized in the band contour. A good example is the AlO (0, 1) band at 5079 Å. The radial velocity obtained from fitting the synthetized spectrum amounts to 52 km s^{-1}. With the increasing rotational number J a new component with a velocity of $\sim$83 km s^{-1} appears, overlapping the blueshifted lines. This pattern repeats in the absorptions from the $v'' = 2$ level. Above $v'' = 2$ the rotational structure is consistent with a velocity of 88 km s^{-1}.
– Redward from the band-head, the rotational pattern seems to be smoothed out, either by a velocity gradient, or by a high density of transitions of the two R-branches, or by both mechanisms.

The rotational contours of the AlO bands are relatively well reproduced if the excitation temperature is of $\sim$1500 K. A similar value was obtained from the AlO bands in the 2005 spectrum (Kamiński et al. 2009). The most significant difference between 2005 and 2009 is the position of the heads of the excited vibrational bands. The present value of 8 km s^{-1} is to be compared with –82 km s^{-1} in 2005.

3.6.6. Summary

The main conclusions that we drawn from the above description of the molecular bands are:

– The excitation temperature of the molecular bands of all observed molecules in 2009 is consistent within the uncertainties with the values derived from the 2005 spectrum.
– Differences in the shape of the molecular bands observed in the two epochs result mainly from the lower column density in 2009, typically by a factor of 2.
– The kinematic structure as inferred from the heads of the molecular bands is generally similar in both epochs.
– Exceptional are the highly excited lines, which are formed at $88 \, \mathrm{km \, s^{-1}}$ in 2009, compared to $57 \, \mathrm{km \, s^{-1}}$ observed in 2005.
– The change in the velocity is most spectacular in the excited AlO bands. In 2009, these heads are at $8 \, \mathrm{km \, s^{-1}}$, whereas in 2005 the head velocities were $-89 \, \mathrm{km \, s^{-1}}$.

4. Conclusions and discussion

Globally, V838 Mon did not significantly evolve between 2005 and 2009. It is now slightly more luminous and hotter than it was in 2005 (Sect. 3.2). It continues to lose matter although at a lower rate. This is indicated by the disappearance of clear emission components in the atomic lines showing P-Cyg profiles in 2005 (Sect. 3).

Several atomic absorption lines display a narrow and faint emission component. Our analysis shows that this is a real emission, most probably a remnant of the P-Cyg emission component observed in 2005, and that its position measures the radial velocity of the object (Sect. 3.5). The peak of the feature is well defined and in all lines, where it is clearly seen, it gives $V_h = 71 \, \mathrm{km \, s^{-1}}$ (equivalent to $V_{LSR} = 54 \, \mathrm{km \, s^{-1}}$), the same value as that of the SiO masers (Deguchi et al. 2005; Claussen et al. 2007). A very similar radial velocity was also measured for a molecular region seen in a near vicinity of V838 Mon in the CO rotational lines (Kamiński et al. 2011). The region is likely to be associated to the dusty matter responsible for the light echo of the 2002 eruption.

An absorption component at radial velocities positive in respect to the systematic velocity of the object (Sect. 3.3 and Fig. 3) is one of the most common features in the atomic lines. This component was also observed in 2005 but was less evident and seen in fewer lines. A likely reason could have been the strong P-Cyg emission component in 2005, which could have filled up the redward absorption in certain lines. But it can also be argued that the redward absorption component became intrinsically stronger in 2009. This is supported by the appearance of a component at $88 \, \mathrm{km \, s^{-1}}$ in the highly excited bands of TiO and other molecules in 2009 (Sect. 3.6).

Similarly as in Tylenda et al. (2009), we interpret the redward absorption component as evidence of infall motions in the atmosphere of V838 Mon. In the present spectrum the maximum of absorption is typically observed at $V_h \simeq 87 \, \mathrm{km \, s^{-1}}$, i.e. at an infall velocity of $\sim 16 \, \mathrm{km \, s^{-1}}$. The long wavelength wing of the feature extends to $V_h \simeq 120 \, \mathrm{km \, s^{-1}}$, indicating a maximum infall velocity of $\sim 50 \, \mathrm{km \, s^{-1}}$. This is consistent with the free-fall velocity for an $8 \, M_\odot$ star (Tylenda et al. 2005) at a photospheric radius of $\sim 400 \, R_\odot$ (Sect. 3.2), which is $\sim 90 \, \mathrm{km \, s^{-1}}$. The infall motions apparently became more intense in 2009. Note that the observed infalls cannot be interpreted as a shrinkage of the V838 Mon remnant. With a velocity of $16 \, \mathrm{km \, s^{-1}}$ it would result in a collapse of the effective radius by a factor of 2 in the course of three months.

The observed kinematics of the AlO bands from the excited levels (sharp heads at $V_h \simeq 8 \, \mathrm{km \, s^{-1}}$ – see Sect. 3.6.5) is not seen in the other molecular bands nor in the atomic line profiles. This suggests that the distribution of aluminium oxide in the photosphere and/or the wind is different from the distributions of the other molecules and atoms. We calculated distributions of Al-bearing molecules in a model stellar atmosphere taken from the MARCS database (Gustafsson et al. 2008) of an effective temperature of 3200 K and log $g = 0.0$. In the computation of the equilibrium composition, equilibrium constants from Tsuji (1973) were used, except AlO and AlO$_2$, for which the data were taken from a parametrization of Sharp & Huebner (1990) of the JANAF data (Chase 1982). The results reveal that in the outer layers of the atmosphere, Al is mainly in the atomic phase. AlO is more than two orders of magnitude less abundant than the atomic Al, and about two orders of magnitude more abundant than AlOH and AlH[8]. A possible explanation of the observed AlO structures is that AlO is additionally produced and exited in processes of non-equilibrium chemistry in a postshock region. This would explain both the presence of the sharp heads and the absorptions from the excited vibrational levels, if the postshock temperature and density were sufficiently high. The position of Hα emission, as seen in Fig. 7, with its blue edge at $\sim 8 \, \mathrm{km \, s^{-1}}$ could also have been explained in this hypothesis.

Absorption features showing the highest outflow velocities, i.e. V_h between -130 and $-50 \, \mathrm{km \, s^{-1}}$, are observed in the molecular bands arising from the ground vibrational level (Sect. 3.6 and Table A.1) and in some atomic lines, mostly in the resonance ones (Fig. 3). With the systematic velocity of the object ($V_h = 71 \, \mathrm{km \, s^{-1}}$), these features imply outflow velocities of $120-200 \, \mathrm{km \, s^{-1}}$. The structures of these high outflow-velocity molecular bands usually give very low excitation temperatures, i.e. of $300-500$ K (Sect. 3.6).

In 2005, a relatively narrow absorption component (NAC) at $V_h \simeq -82 \, \mathrm{km \, s^{-1}}$ was observed in RbI $\lambda \, 7800$ and MgI $\lambda \, 4571$ (see Fig. 6 in Kamiński et al. 2009). These two lines are, unfortunately, outside the spectral range of the 2009 spectrum. However, a similar component at practically the same velocity is now observed in CaI $\lambda \, 6572$ and LiI $\lambda \, 6708$ (see panel a in Figs. 3 and 4).

In Tylenda et al. (2009), all features in the atomic lines were intepreted in terms of a standard spherically symmetric wind model. Within this model, the NAC would have originated from a local density maximum in the wind, produced by a short-lived high mass-loss event. A jet-like structure in the ongoing mass outflow was considered as another possible explanation of the NAC. A third possibility was that the NAC had nothing to do with the current mass outflow from V838 Mon, but instead it was formed in a distant matter ejected by V838 Mon during the 2002 eruption. This last explanation was rejected mainly on an argument raised from a discussion of the TiI lines. That argument was incorrect, however, since the excitation energy of the upper level of the TiI lines was mistaken as that of the lower level in Tylenda et al. (2009). Below we show that the 2002 ejecta is the only reasonable explanation not only of the NAC, but probably of all the absorption features observed at high outflow velocities.

A short-lived mass-loss event in the ongoing mass outflow can immediately be rejected in view of Sect. 3.4 and Fig. 4. In the standard wind model of Tylenda et al. (2009), the shell producing the NAC was at ~ 2 radii of the central star. Therefore, the feature should have evolved on a time scale of ~ 20 days.

---

[8] The differences with previous computations (e.g. Tenenbaum & Ziurys 2009) that predicted a much lower concentration of AlO are caused by the newer equilibrium constants used in our modelling.

The features at $V_h \lesssim -50$ km s^{-1} in the CaI and LiI lines were very stable over a time span of almost three months. A jet-like outflow could in principle produce a stable feature at the projected velocity of the jet. However, it is not clear how it could produce such a complex and stable structure as that observed in the LiI λ 6708 (condensations in the jet would flow out on a time scale of days). Besides, as noted above, the molecular bands displaying high outflow velocities show very low excitation temperatures, so they cannot be formed close to the photosphere of V838 Mon.

During the time span between our individual observations in 2009, matter flowing with a velocity of ~150 km s^{-1} covered a distance of ~1500 $R_\odot$, i.e. ~4 radii of the V838 Mon remnant (see Sect. 3.2). Therefore, the only reasonable way of explaining the observed stability of the high outflow velocity features in the CaI λ 6572 and LiI λ 6708, as well as of the narrow absorptions at $V_h = -92$ km s^{-1} in the BaI, BaII, and TiI lines (see panels b and c in Fig. 3), is to conclude that the above estimated distance of ~1500 $R_\odot$ is negligible compared to the distance of matter in which the features are formed. On the other hand, comparing the line profiles observed in 2009 with those observed in 2005, we see that the discussed features evolve on a time scale of years. The conclusion is quite clear: the high-velocity features are formed in the matter ejected by V838 Mon in 2002. During the 2002 eruption the observed outflow velocities were between ~100 and ~600 km s^{-1} (Munari et al. 2002a; Crause et al. 2003; Kipper et al. 2004). The most intense mass loss probably took place at the end of the eruption, i.e. in March 2002 (Tylenda 2005), with outflow velocities ranging from ~100 to ~300 km s^{-1} (Crause et al. 2003; Tylenda 2005). In the 2005 and 2009 spectra, we thus observe relatively slow but dense parts of the 2002 ejecta. Faster and presumably less dense regions quickly became too thin to be observable.

The above hypothesis follows Lynch et al. (2004, 2007), who concluded from their earlier observations that strong molecular bands observed in the near-IR were formed in the expanding 2002 ejecta. It explains several observational facts from our observations that are not easily understood otherwise, i.e. abnormaly strong molecular bands in the spectrum of V838 Mon when compared to typical giants or supergiants of a similar spectral type, very low excitation temperatures of the molecular bands formed at high outflow velocities, and decrease in the column densities observed in the high velocity molecular bands between 2005 and 2009 (Sect. 3.6). It is now clear also why the maximum observed outflow velocity of 215 km s^{-1} was the same in 2005 and 2009 and removes problems with explaining that high value in terms of the winds from cool giants (Tylenda et al. 2009).

From the low-excitation TiO and VO bands observed in the October 2005, Kamiński et al. (2009) derived a column density of H atoms of ~24 dex cm^{-2}, i.e. ~2 g cm^{-2}. If the matter had been lost in March 2002 with a velcity of 150 km s^{-1}, it would have been at a distance of ~2.5×10^4 $R_\odot$ in October 2005. Assuming spherical symmetry, one obtains a mass of the expanding shell of ~0.04 $M_\odot$. This result agrees well with an estimate of the expanding mass made in Lynch et al. (2004) and is within the limits of the mass lost by V838 Mon in the 2002 eruption obtained in Tylenda (2005).

The disappearance of the B3 V companion from the spectrum of V838 Mon is the most intriguing event in the recent years' history of the object. It started with an eclipse-like event in November−December 2006 (Munari et al. 2007). Then the companion reappeared in the spectrum for a few months and next started a slower but deeper and more complex decline. Note that after the 2002 eruption the U brightness of V838 Mon was dominated by the B3 V companion. Our spectroscopy shows that in 2009 the B3 V companion was at least 30 times fainter in the optical than in 2005 (Sect. 3.1). Following the interpretation of Tylenda et al. (2009), we can conclude that the B3 V companion is now engulfed in a dense dusty cloud of matter lost by V838 Mon during the 2002 eruption. The luminosity of the companion is thus expected to be now reemitted in the infrared. Therefore, one should look for traces of the companion in IR observations. This can appear to be a hard task, however, since the luminosity of the B3 V companion was only of a few per cent of that of the V838 Mon remnant.

Given that the B3 V companion has already disappeared for a few years, one can speculate that in 2007 the companion entered the V838 Mon remnant and is now completely engulfed in the remnant itself. This idea would imply a second merger phase in the history of V838 Mon, in which the B3 V companion would finally merge with the core of V838 Mon. This would result in a much more energetic and dramatic event than the 2002 eruption. We do not follow this speculation any further, as it does not seem very likely in view of the observational facts. Since its discovery in October 2002 until the eclipse-like event in 2006, the spectrum of the B3 V companion showed no interactions of the star with the 2002 ejecta. In particular, the U brightness, dominated by the B3 V companion in that epoch, remained virtually constant.[1] This shows that the companion is at a significant distance from V838 Mon, so that the matter ejected in 2002 was not able to interact with the companion until it reached the star at some point in 2006.

Future observations will distinguish between the two scenarios. It is very likely that V838 Mon has not yet finished to suprise us. Undoubtedly, the object deserves further observational monitoring.

Appendix A: Molecular bands in the spectrum of V838 Mon observed in 2009

A detailed identification of the molecular features in the spectrum of V838 Mon was made in (Kamiński et al. 2009, see their Table 3). The list of the molecular bands observed in 2009 remains practically the same as in 2005. Table A.1 presents details of those molecular bands observed in the spectrum of V838 Mon in 2009 for which we were able to estimate the radial velocity. First column displays the observed wavelengths of the bands, while their laboratory wavelengths are given in the second column. Identification details of the bands are presented in the third column. Heliocentric radial velocities of the bands are given in the fourth column. Three different methods were used to derive the velocities, as indicated in the last column of the table. The meanings of the symbols are as follows: M5 III – comparison of the V838 Mon spectrum to the UVES spectrum of an M5 III star HD118767 (Bagnulo et al. 2003); LAB – direct comparison of the band head position with the laboratory measurements (see Kamiński et al. 2009, for laboratory data sources); SYNTH - spectral synthesis of the bands as described in Kamiński et al. (2009).

Table A.1. Heliocentric radial velocities of the molecular bands in the 2009 spectrum of V838 Mon.

λ_{obs} (Å)	λ_{lab} (Å)	Identification	Velocity (km s^{-1})	Method
4788−4804		TiO α (2, 0) high J tail	+88 ± 5	M5 III
4805.2	4804.333	TiO α (3, 1) R$_2$	+56 ± 25	LAB
4831−4841		TiO α (3, 1) high J tail	+88 ± 5	M5 III
4842.47	4842.27	AlO B$^2\Sigma$–X$^2\Sigma$ (0, 0) R$_2$	+12 ± 10	LAB
4889.26	4889.0	AlO B$^2\Sigma$–X$^2\Sigma$ (2, 2) R$_2$	+16 ± 10	LAB
4953.0 ± 0.2	4954.592	TiO α (1, 0)	−90 ± 18	LAB
4993−4998		TiO α (1, 0) high J tail	+88 ± 10	M5 III
5042−5078		TiO α (3, 2)	+88 ± 10	M5 III
5079.5	5079.36	AlO B$^2\Sigma$–X$^2\Sigma$ (0, 1)	+8 ± 5	LAB
5087−5096		AlO B$^2\Sigma$–X$^2\Sigma$ (0, 1) P-branch	+52 ± 5	SYNTH
5102.3	5102.13	AlO B$^2\Sigma$–X$^2\Sigma$ (1, 2) R-head	+10 ± 5	LAB
5113−5118		AlO B$^2\Sigma$–X$^2\Sigma$ (1, 2) P-branch	+52 ± 5	SYNTH
5123.6	5123.33	AlO B$^2\Sigma$–X$^2\Sigma$ (2, 3) R-head	+15 ± 6	LAB
5143.3	5142.89	AlO B$^2\Sigma$–X$^2\Sigma$ (3, 4) R-head	+23 ± 10	LAB
5130−5137		AlO B$^2\Sigma$–X$^2\Sigma$ (3, 4) high-J	+88 ± 10	SYNTH
5164.4	5166.450	TiO α (0, 0) R$_2$	−119 ± 10	LAB
5197−5203		TiO α (0, 0) high-J	+88 ± 10	LAB
5213−5225		TiO α (0, 0) high-J	+88 ± 10	LAB
5226.3	5228.2	VO C-X (2, 0) R-head	−109 ± 10	LAB
5228.0	5228.2	VO C-X (2, 0) R-head	+11 ± 10	LAB
	5240.463	TiO f$^1\Delta$-a^1 (0, 0)	+88 ± 10	M5 III
	5259.418	TiO α (2, 2) R$_2$	+88 ± 10	M5 III
	5275.8	VO C-X (3, 1)	+88 ± 10	M5 III
	5307.116	TiO α (3, 3)	+88 ± 10	M5 III
5377.21	5376.813	AlO B$^2\Sigma$-X$^2\Sigma$ (2,4)	+22 ± 10	LAB
5467.7	5469.3	VO C-X (1, 0)	−88 ± 10	LAB
5468.3	5469.3	VO C-X (1, 0)	−52 ± 10	LAB
5488−5498		TiO α (0, 1) high-J	+88 ± 10	M5 III
	5496.423	TiO α (1, 2) R$_2$	+88 ± 10	M5 III
5512−5525		TiO α (1, 2) high-J	+88 ± 10	M5 III
		TiO β (0, 0)	+88 ± 10	M5 III
		TiO β (1, 1)	+88 ± 10	M5 III
		TiO β (2, 2)	+88 ± 10	M5 III
5650−5660		TiO γ (3, 1) high-J tail	+88 ± 10	M5 III
	?5712.6	TiO γ' (4, 2)	+88 ± 10	M5 III
	?5717.0	TiO γ' (4, 2)	+88 ± 10	M5 III
5735.22	5736.703	VO C-X (0, 0)	−78 ± 10	LAB
5735.98	5736.703	VO C-X (0, 0)	−38 ± 10	LAB
	5758.741	TiO α (0, 2) R$_2$	+88 ± 10	M5 III
5845.73	5847.593	TiO γ' (1, 0) R$_1$	−97 ± 10	LAB
5950		TiO γ' (2, 1) R$_3$	+88 ± 10	M5 III
5999.64	6001.151	TiOγ (3, 0) R$_2$	−75 ± 10	LAB
	6064.31	ScO (0, 0) R$_1$	+88 ± 10	M5 III
6077.65	6079.30	ScO (0, 0) Q$_1$	−81 ± 20	LAB
6147.15	6148.68	TiO γ' (0, 0) ^{S}R$_{21}$	−75 ± 10	LAB
6269.3	6268.86	TiO γ' (1, 1)	+18 ± 10	M5 III
6292.2	6294.80	TiO γ (2, 0) R$_3$	−123 ± 20^a	LAB
6294.2	6294.80	TiO γ (2, 0) R$_3$	−29 ± 10^a	LAB
6296.0	6294.80	TiO γ (2, 0) R$_3$	+57 ± 5^a	LAB
6318.9	6321.21	TiO γ (2, 0) R$_2$	−110 ± 10^a	LAB
6320.7	6321.21	TiO γ (2, 0) R$_2$	−24 ± 10^a	LAB
6349.7	6351.29	TiO γ (2, 0) R$_1$	−75 ± 20^a	LAB
6398-6412		TiO γ (3, 1) high-J tail	+88 ± 10	M5 III
	6447.90	TiO γ (4, 2)	+88 ± 10	M5 III
	6478.55	TiO γ (4, 2) R$_1$	+88 ± 10	M5 III
	6512.409	TiO γ (5, 3) R$_2$	+88 ± 10	M5 III
	6543.950	TiO γ (5, 3) R$_1$	+88 ± 10	M5 III
	6549.600	TiO γ (6, 4) R$_3$	+88 ± 10	M5 III
	6577.716	TiO γ (6, 4) R$_2$	+88 ± 10	M5 III
6649.34	6651.252	TiO γ (1, 0) R$_3$	−86 ± 20	LAB
6678.81	6680.796	TiO γ (1, 0) R$_2$	−89 ± 20	LAB
6712.59	6714.477	TiO γ (1, 0) R$_1$	−84 ± 20	LAB
	6717.578	TiO γ (2, 1) R$_3$	+68 ± 5	M5 III

Table A.1. continued.

λ_{obs} (Å)	λ_{lab} (Å)	Identification	Velocity (km s^{-1})	Method
6733–6740		TiO γ (1, 0) high-J tail	$+68 \pm 5$	M5 III
	6747.589	TiO γ (2, 1) R$_2$	$+68 \pm 5$	M5 III
6765–6780		TiO γ (2, 1) high-J tail	$+88 \pm 5$	M5 III
6808–6815		TiO γ (2, 1) high-J tail	$+88 \pm 5$	M5 III

Notes. [a] No clear bandhead, a velocity gradient in the profile is observed.

References

Afsar, M., & Bond, H. E. 2007, AJ, 133, 387
Antonini, F., Montez, R. Jr., Kastner, J., et al. 2010, ApJ, 717, 795
Bagnulo, S., Jehin, E., Ledoux, C., et al. 2003, The Messenger, 114, 10, see also, http://www.sc.eso.org/santiago/uvespop/field_stars_uptonow.html
Barsukova, E., Goranskij, V., Abolmasov, P., & Fabrika, S. 2006, ATel, 803
Berger, E., Soderberg, A. M., Chevalier, R. A., et al. 2009, ApJ, 699, 1850
Bond, H. E., Henden, A., Levay, Z. G., et al. 2003, Nature, 422, 405
Bond, H. E., Bedin, L. R., Bonanos, A. Z., et al. 2009, ApJ, 695, L154
Casali, M. M., & Hawarden, T. G. 1992, JCMT-UKIRT Newsletter, 3, 33
Chase, M. W. 1982, JANAF Thermodynamical Tables, Magnetic Tape Version (Midland, MI: Dow Chemical Co.)
Claussen, M. J., Bond, H. E., Starrfield, S., & Healy, K. 2007, in The Nature of V838 Mon and its Light Echo, ed. R. L. M. Corradi, & U. Munari, ASP Conf. Ser., 363, 87
Crause, L. A., Lawson, W. A., Kilkenny, D., et al. 2003, MNRAS, 341, 785
Deguchi, S., Matsunaga, N., & Fukushi, H. 2005, PASJ, 57, L25
Dekker, H., D'Odorico, S., Kaufer, A., Delabre, B., & Kotzlowski, H. 2000, Proc. SPIE, 4008, 534
Geballe, T. R., Rushton, M. T., Eyres, S. P. S., et al. 2007, A&A, 467, 269
Gustafsson, B., Edvardsson, B., Eriksson, K., et al. 2008, A&A, 486, 951
Hamuy, M., Walker, A. R., Suntzeff, N. B., et al. 1992, PASP, 104, 533
Hamuy, M., Suntzeff, N. B., Heathcote, S. R., et al. 1994, PASP, 106, 566
Iben, I., & Tutukov, A. V. 1992, ApJ, 389, 369
Kamiński, T., Miller, M., & Tylenda, R. 2007, A&A, 475, 569
Kamiński, T., Schmidt, M., Tylenda, R., Konacki, M., & Gromadzki, M. 2009, ApJS, 182, 33
Kamiński, T., Schmidt, M., & Tylenda, R. 2010, A&A, 522, A75
Kamiński, T., Tylenda, R., & Deguchi, S. 2011, A&A, 529, A48
Kashi, A., & Soker, N. 2010 [arXiv:1011.1222]
Kashi, A., Frankowski, A., & Soker, N. 2010, ApJ, 709, L11
Kipper, T., Klochkova, V. G., Annuk, K., et al. 2004, A&A, 416, 1107
Kulkarni, S. R., Ofek, E. O., Rau, A., et al. 2007, Nature, 447, 458
Lawlor, T. M. 2005, MNRAS, 361, 695
Levesque, E. M., Massey, P., Olsen, K. A. G., et al. 2005, ApJ, 628, 973
Lynch, D. K., Rudy, R. J., Russell, R. W., et al. 2004, ApJ, 607, 460
Lynch, D. K., Rudy, R. J., Russell, R. W., et al. 2007, in The Nature of V838 Mon and its Light Echo, ed. R.L.M. Corradi, & U. Munari, ASP Conf. Ser., 363, 39
Martini, P., Wagner, R. M., Tomaney, A., et al. 1999, AJ, 118, 1034
Mason, E., Diaz, M., Williams, R. E., Preston, G., & Bensby, T. 2010 A&A, 516, A108
Mould, J., Cohen, J., Graham, J. R., et al. 1990, ApJ, 353, L35
Munari, U., Henden, A., Kiyota, S., et al. 2002a, A&A, 389, L51
Munari, U., Desidera, S., & Henden, A. 2002b, IAU Circ., 8005
Munari, U., Corradi, R. L. M., Henden, A., et al. 2007, A&A, 474, 585
Richichi, A., Fabbroni, L., Ragland, S., & Scholz, M. 1999, A&A, 344, 511
Schmidt-Kaler, Th. 1982, Landolt-Börnstein: Numerical Data and Functional Relationships in Science and Technology, ed. K. Schaifers, & H. H. Voigt (Berlin: Springer-Verlag), VI/2b
Sharp, C. M., & Huebner, W. F. 1990, ApJS, 72, 417
Sparks, W. B., Bond, H. E., Cracraft, M., et al. 2008, AJ, 135, 605
Tenenbaum, L. D., & Ziurys, L. M. 2009, ApJ, 694, L59
Tsuji, T. 1973, A&A, 23, 411
Tylenda, R. 2005, A&A, 436, 1009
Tylenda, R., & Soker, N. 2006, A&A, 451, 223
Tylenda, R., Soker, N., & Szczerba, R. 2005, A&A, 441, 1099
Tylenda, R., Kamiński, T., & Schmidt, M. 2009, A&A, 503, 899
Tylenda, R., Hajduk, M., Kamiński, T., et al. 2011, A&A, 528, A114
van Dokkum, P. G. 2001, PASP, 113, 1420
Willmarth, D., & Barnes, J. 1994, A User's Guide to Reducing Echelle Spectra With IRAF (Tucson: NOAO), http://iraf.net/irafdocs/ech/